Shock Waves (2026) 36:2
https://doi.org/10.1007/s00193-026-01261-9

ORIGINAL ARTICLE

Two-dimensional numerical simulation of imploding detonations

L. Shi[1] · E. Fan[1] · C.-Y. Wen[1]

Received: 21 October 2025 / Revised: 6 January 2026 / Accepted: 7 January 2026

Abstract
This study aims to contribute to the understanding of imploding detonations from a numerical perspective, focusing primarily on the detailed transient and wave structures during implosion that are challenging to capture experimentally. An inviscid perfect gas model with a single-step Arrhenius reaction is employed. Imploding detonations are initiated by collisions of multiple small hot spots, and both two-dimensional circular and polygonal implosions are examined, with attention to the effects of obstacles and varying ignition pressures. For circular implosions, a slight acceleration of detonation velocity is observed at ignition, with significant acceleration occurring only in the final stages. Near the implosion center, local wave velocities exceed twice the Chapman–Jouguet velocity, yet the wave front maintains cellular instabilities until the collapse is complete. Additionally, the merging of transverse waves is observed during the implosion. In polygonal cases, a small number of "ignition edges" allows regular reflection, preserving the initial wave front geometry, while increasing the number of ignition lines leads to Mach reflection and the formation of a circular wave front. When obstacles are introduced, the detonation reflects off the obstacle, causing localized delays in the wave front that cannot be fully compensated, as transverse waves are unable to propagate sufficiently in the circumferential direction to smooth out disturbances. Similar effects are noted for implosions with non-uniform ignition pressures. It should be noted that the findings are based on a simplified model and do not account for real gas effects or additional physical processes present in actual detonation implosions.

Keywords Detonation · Implosion · Cylindrical detonation · Cellular instability · Mach reflection

1 Introduction

During the implosion of an inert cylindrical shock wave, the inward acceleration can create extreme thermal conditions, potentially approaching a singularity at the center. It has been demonstrated that light is emitted near the center of the collapse during the implosion of a two-dimensional (2D) inert shock wave [1, 2]. In the context of an imploding detonation, a strongly overdriven detonation approaches a strong shock very close to the global implosion center, as the heat release at the front is relatively small compared to the mechanisms of area convergence [3]. However, in the case of multidimensional imploding detonations, it remains uncertain how inherent cellular instabilities might affect the degree of accumulation at the core.

Early pioneering studies, such as those conducted by Knystautas and Lee [4, 5] and Ahlborn and Huni [6], have been fundamental in shaping the understanding of detonation wave implosions. In a successful implosion apparatus [5], detonation was initiated by spark ignition in the annulus at one end of a co-axial tube. When it emerges, it diffracts, producing a cylindrical detonation wave that converges toward the center of the test section. Disturbances are further introduced by placing a small cylindrical obstacle within the test section, which causes the detonation wave to reflect and diffract around the obstacle. Initially, these disturbances are pronounced, and the local wave front lags behind the surrounding wave fronts. However, as the wave approaches the center, these disturbances are gradually smoothed out. This phenomenon was referred to as the "curvature distribution mechanism," where local perturbations are redistributed around the detonation front by transverse waves [5].

Communicated by G. Ciccarelli.

This paper is based on work that was presented at the 30th International Colloquium on the Dynamics of Explosions and Reactive Systems (ICDERS), Ottawa, Canada, July 27–August 1, 2025.

✉ C.-Y. Wen
chihyung.wen@polyu.edu.hk

[1] Department of Aeronautical and Aviation Engineering, The Hong Kong Polytechnic University, Hung Hom, Hong Kong

Published online: 02 March 2026

Theoretically, Li and Ben-Dor [7] developed an area-Mach number relation for detonation waves, based on a similar concept for inert shock waves proposed by Whitham [8]. According to the model, significant acceleration is expected only near the implosion center, and the velocity profile as a function of radius is highly sensitive to even minor variations in the initial velocity. More recently, Rodriguez Rosero et al. [9] revisited this topic through a series of experiments, investigating the mechanisms responsible for asymmetric implosion. This was achieved by intentionally canting the width of the test section at a small angle, enabling the observation of asymmetries. Their theoretical results, based on the assumption that the local detonation velocity depends on boundary-layer displacement, aligned with the observed experimental offsets. These findings confirmed that momentum losses to the walls of the thin channel are the primary cause of asymmetry.

Oran and DeVore [10] conducted a numerical study of cylindrically imploding detonations with various assumptions regarding the reaction models, achieving quantitative agreement with the Chester-Chisnell-Whitham theory. Their simulations, which covered both symmetrical and perturbed detonation implosions, used a relatively coarse mesh resolution. In the present study, the objective is to extend the previous findings through the application of more advanced numerical techniques. The present approach ensures that the domain is sufficiently large and allows precise capture of cellular instabilities. Additionally, it aims to provide a thorough understanding of the implosion process, with particular emphasis on the final collapse.

2 Physical modeling

The numerical simulation of detonation implosion remains a largely underexplored area, and the influence of the initial ignition process on the final outcomes of detonation implosion is not well understood. Furthermore, the use of detailed chemical models is computationally prohibitive, as the simulation domain may encompass thousands of detonation cells. More critically, the thermal conditions near the implosion center may exceed the capabilities of conventional thermodynamic models. Although such high-cost and complex simulations may be challenging to implement at present, they could become feasible once the general behavior of detonation implosion is better understood.

In light of these considerations, this study adopts a simplified reaction model, specifically a one-step chemical reaction model. This model has been extensively employed in multidimensional, large-scale detonation simulations, such as those involving cylindrical diverging detonations [11, 12], inhomogeneous detonations in semi-confined channels [13], and three-dimensional detonation structures [14]. We follow the governing equations outlined in [11–14], which employ nondimensional forms, a one-step reaction model, and neglect viscous effects. The two-dimensional reactive Euler equations are expressed as follows:

$$\frac{\partial \mathbf{U}}{\partial t}+\frac{\partial \mathbf{F}(\mathbf{U})}{\partial x}+\frac{\partial \mathbf{G}(\mathbf{U})}{\partial y}=\mathbf{S}$$

with

$$\mathbf{U}=\begin{bmatrix}\rho\\ \rho u\\ \rho v\\ E\\ \rho\lambda\end{bmatrix},\quad \mathbf{F}=\begin{bmatrix}\rho u\\ \rho u^2+p\\ \rho uv\\ (E+p)u\\ \rho\lambda u\end{bmatrix},$$

$$\mathbf{G}=\begin{bmatrix}\rho v\\ \rho vu\\ \rho v^2+p\\ (E+p)v\\ \rho\lambda v\end{bmatrix},\quad \mathbf{S}=\begin{bmatrix}0\\ 0\\ 0\\ 0\\ \dot{\omega}\end{bmatrix},$$

where ρ, p, u, v, λ, and E denote dimensionless density, pressure, the fluid velocities in the x and y directions, the mass fraction of the reactant, and the total energy per unit volume, respectively. The chemical reaction rate follows the Arrhenius equation $\dot{\omega}=-K\rho\lambda\exp\left(-E_{\mathrm{a}}/T\right)$, where E_{a} is the activation energy and K is a scaling factor adjusted to ensure that the ZND half-reaction length $\left(\ell_{1/2}\right)$ is of unit length scale. The ideal gas law in nondimensional form is written as $p=\rho T$, and the total energy per unit volume is given by $E=p/(\gamma-1)+\frac{1}{2}\rho\left(u^2+v^2\right)+\lambda\rho Q$, where Q represents the heat released by chemical reaction. The dimensionless forms of variables with respect to the state of the unburned gas are given by:

$$\rho=\frac{\rho'}{\rho_0'},\ p=\frac{p'}{p_0'},\ T=\frac{T'}{T_0'},\ u=\frac{u'}{\sqrt{RT_0'}},\ v=\frac{v'}{\sqrt{RT_0'}}$$

$$E_{\mathrm{a}}=\frac{E_{\mathrm{a}}'}{RT_0'},\ Q=\frac{Q'}{RT_0'},\ x=\frac{x'}{\ell_{1/2}'},\ t=\frac{t'}{\ell_{1/2}'/\sqrt{RT_0'}},$$

where R is the gas constant. The variable with a prime indicates its dimensional form, and the one with a subscript 0 indicates the corresponding value of the unburned gas.

A key assumption in the present study is that, at or near the onset of implosion, the detonation front is cellular rather than planar. Additionally, it is assumed that the distribution of these cellular instabilities retains some anisotropy, i.e., not all cellular structures from every direction are perfectly in phase shortly after ignition. These assumptions are consistent with the behavior observed in experiments. In contrast, if the

detonation wave were initialized as perfectly planar and the propagation distance did not allow for the development of cellular structures, the scenario would resemble quasi-1D rather than 2D detonation implosion.

To model this, we set the activation energy E_a to 27, representing a weakly unstable gas mixture. The imploding detonation is ignited by numerous small hot spots. The size of these ignition bubbles is chosen to be smaller than the detonation cell size, which allows for the self-generation of natural cellular structures in the simulation. The other parameters chosen are $\gamma = 1.2$ and $Q = 50$, which correspond to a Chapman–Jouguet (CJ) detonation velocity of $D_{CJ} = 6.81$. The unreacted quiescent gas is initialized with a pressure of 1 and a temperature of 1.

Figure 1 presents a schematic of a sample hexagonal implosion to illustrate the computational setup. The reactive gas is surrounded by hexagonal ignition sources (with $n = 6$ edges), while the inert gas with a pressure of 1 and a temperature of 1 occupies the outer region. The distance from the center to the edge of the ignition source, denoted as r, is kept constant at 700 unit lengths for all cases in the present study. The center of the domain, which represents the anticipated global implosion center for a perfectly symmetrical implosion, is located at $(x, y) = (0, 0)$. Small hot spots are attached one by one with no spacing in-between and are arranged in a linear pattern to create a line of ignition sources, with several such lines (n) collectively creating the initial polygonal detonation. By default, the temperature for these ignition spots is set to 10, the pressure to $p_{ig} = 60$, $\lambda = 1$, and the radius to 5. This set of ignition parameters was selected somewhat arbitrarily, primarily to ensure that the gas can be directly detonated. Meanwhile, a case with a higher ignition pressure is also considered to investigate its influence. By arranging the positions of these small ignition bubbles, the present study investigates both cylindrical symmetric (circular) and polygonal ignition configurations.

Additionally, it is important to emphasize that the entire domain is simulated, rather than a quarter of it, to avoid potential boundary-related issues. The phenomenon might not be perfectly symmetrical, particularly near the center, as we do not assume symmetry a priori. Simulating the full domain also helps mitigate numerical challenges associated with setting appropriate boundary conditions for sharp corners. Inspired by previous works [5, 10], a circular obstacle is introduced in some cases to artificially trigger disturbances. The center of this obstacle is fixed at $(x, y) = (350, 350)$.

The simulations are conducted using the block-structured adaptive mesh refinement (AMR) solver for combustion, PeleC [15]. The piecewise parabolic method (PPM) [16] is employed to reconstruct values at the cell faces, and an iteratively coupled scheme based on the spectral deferred correction (SDC) approach [17] is used to advance the system through each numerical time step. The present solver has been validated through channel detonation simulations for both stable and mildly unstable detonations, producing cell sizes and regularities that align with the findings reported in reference [18]. Based on the temperature and density gradients, three levels of mesh refinement are applied to adaptively refine the mesh around the leading detonation waves and transverse waves, with the finest level of resolution set to $10\,\text{pts}/\ell_{1/2}$ (i.e., $\Delta x = 1/10$) for most cases. Higher resolutions, up to $80\,\text{pts}/\ell_{1/2}$, are used for the benchmark case, although no significant differences are observed for the concerns addressed in this study. Simulations are performed on the Tianhe supercomputer at the Tianjin Supercomputer Center, China.

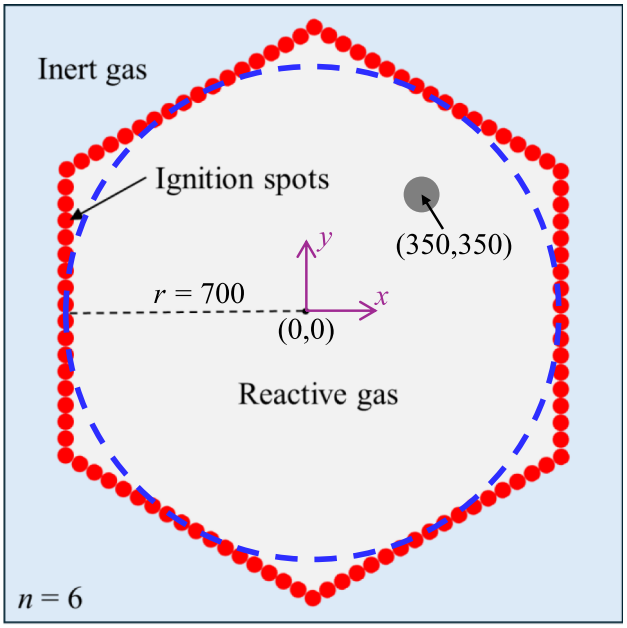

Fig. 1 Schematic of the numerical setup. The small red circles (not to scale) represent ignition hot spots, arranged to form a hexagonal implosion. The blue dashed circle indicates the locations of ignition spots for the circular ignition cases. The gray solid circle denotes the obstacle used to trigger large disturbances in certain cases

3 Results

In total, 14 cases were investigated, as listed in Table 1, varying the number of ignition sources, obstacle size, and other specific settings. The first group (cases 1–3) represents the circular implosion benchmark, which receives greater emphasis. The remaining cases examine the effects of ignition energy (case 4), ignition shapes (cases 5–7), obstacles (cases 8–12), and non-uniform ignition (cases 13 and 14).

Table 1 Key parameters for each case

Case	Side no. (n)	r_{obs}	Specific setting
1	–	–	–
2	–	–	$\Delta x = 1/20$
3	–	–	$\Delta x = 1/80$
4	–	–	$p_{\text{ig}} = 90$
5	3	–	–
6	6	–	–
7	18	–	–
8	–	25	–
9	–	50	–
10	–	100	–
11	9	50	–
12	18	50	–
13	18	–	$p_{\text{ig}} = 90$ for quadrant I
14	18	–	$p_{\text{ig}} = 120$ for quadrant I

The parameter r_{obs} denotes the obstacle radius. The default resolution is $\Delta x = 1/10$, and the ignition pressure is $p_{\text{ig}} = 60$

3.1 Circular implosion benchmark

3.1.1 Overview of wave structures

The analysis begins with Case 1, where circular ignition sources are applied. The instantaneous implosion process of detonation is described in Appendix 1. As observed, the interaction of neighboring ignition bubbles facilitates the formation of the detonation front. This multi-headed detonation front converges symmetrically before reflecting, resulting in the formation of a highly dense region. Figure 2 presents the numerical soot foil obtained during the implosion, revealing the cellular structure of the wave propagation. As seen in subsequent figures, cross-lines are employed to assist in identifying the absolute center of the computational domain. Notably, the simulation domain is sufficiently large, encompassing multiple detonation cells from the ignition source to the center, thereby approximating the high-pressure conditions observed in experimental setups [5, 9]. The small cells near the outermost region are induced by the perturbation from high-pressure ignition sources. These small cells require some distance to relax, allowing them to develop a natural cellular structure and eliminate the initial ignition wavelength.

In the enlarged view shown in Fig. 2, two dashed blue lines are included to illustrate that during the implosion process transverse waves do not merely accumulate in number but merge. Given the mild irregularity of the cellular structure, the wave count is conducted manually from shortly after ignition until near the center. As illustrated in Fig. 3, the number of transverse waves (n) decreases as the wavefront approaches the center. The detonation cell number density, defined as the number of detonation cells per unit wavefront length, is computed as $\lambda^{-1} = \frac{n}{2} \cdot \frac{1}{2\pi|r|}$. Notable variations in λ^{-1} during the range $r \approx -700$ to -450 indicate that the initial decrease in the number of transverse waves within this range is primarily due to the transition from small ignition bubbles to the intrinsic cell size. Following this phase, a plateau in cell number density λ^{-1} is observed from $r \approx -450$ to -150, with the near-constant cell size likely resulting from minimal acceleration, as depicted in the instantaneous velocity profile shown in Fig. 4b, even though the detonation remains slightly overdriven. Within this nearly constant velocity range, transverse waves merge as r decreases, thereby facilitating the maintenance of a consistent cell size. As the implosion center is approached (from $r \approx -150$ to 0), the detonation becomes strongly overdriven, leading to a rapid increase in cell number density λ^{-1}. This increase may result from a combination of rapid transverse wave accumulation, where n continues to decrease as transverse waves merge, and wave fronts significantly accelerate. Importantly, the value of n does not tend toward zero as r approaches 0.

Despite the reduction in wave number, the wave number density per unit area increases. Furthermore, the two arrowed dashed lines highlight the trajectories of two triple points, indicating regions where information from a specific point can be transmitted. A more detailed analysis of these regions will be presented later.

3.1.2 Simulation results with finer mesh resolutions

The influence of mesh resolution on the simulation results is reported herein. The soot foil in Fig. 4a corresponds to a simulation with a resolution of 20 pts/$\ell_{1/2}$ (Case 2). The general observations remain largely unchanged. A much higher resolution simulation (80 pts/$\ell_{1/2}$, Case 3) was performed using an intermediate time result from the coarser resolution, focusing on an area with a radius of 120 near the center, as indicated by the dashed circle in Fig. 4a. Without this restriction, the simulation would have taken an impractically long time to complete.

Figure 5 provides a comparison of the zoomed-in density contours at $t = 90$ and the corresponding soot foil images across three different mesh resolutions. No significant differences are observed qualitatively. Moreover, as presented in Fig. 3 quantitatively, the results obtained at 20 pts/$\ell_{1/2}$ indicate a slight delay in the transition of the detonation from initial bubble sizes to the natural cell size. However, it is evident that the detonation cell number density from $r \approx -400$ to -150 is in good agreement with the results from the 10 pts/$\ell_{1/2}$ resolution. More importantly, all three resolutions exhibit closely matched curves for both n and

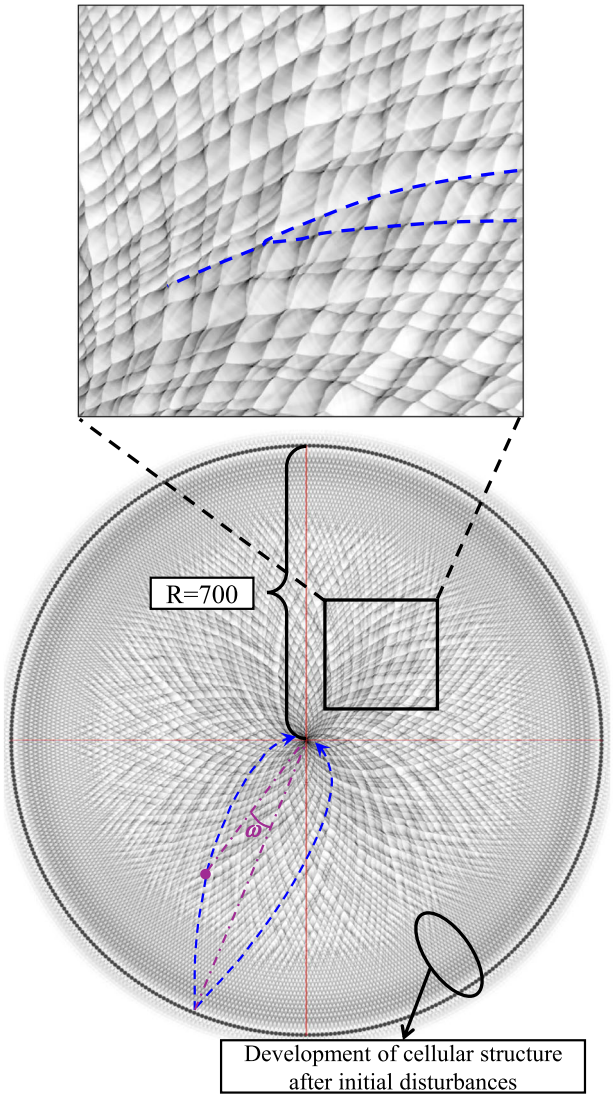

Fig. 2 Soot foil for the benchmark (Case 1). The blue dashed lines represent sample trajectories of triple points as they propagate toward the center. The red cross-lines mark the exact center of the computational domain. The parameter ω denotes the angle from a point along the trajectory relative to the center

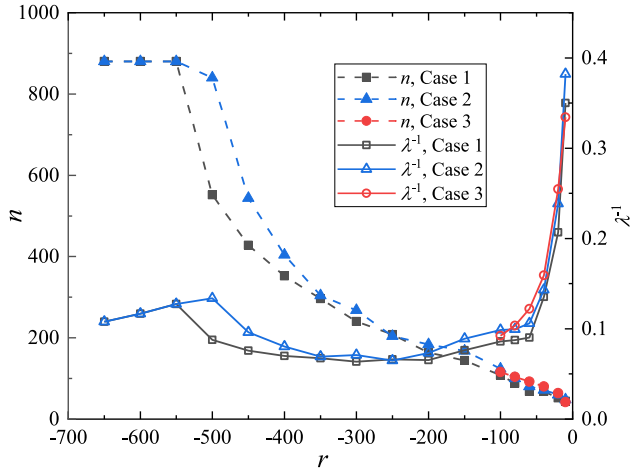

Fig. 3 The number of transverse waves (n) at the detonation front and the cell number density (λ^{-1}) at different radial locations

λ^{-1} during the final acceleration stage, thereby validating the adequacy of the mesh resolution utilized in the present study.

To analyze the velocity profile, we consider an arbitrary line extending from the ignition point to the center. Specifically, the line from $(-700, 0)$ to $(0, 0)$, and plot the instantaneous velocity as a function of radius in Fig. 4b. The observed fluctuations are attributed to cellular instabilities. A rapid acceleration is observed as the wave approaches the center. In fact, a closer examination of the radius-time plot in Fig. 4c reveals that the acceleration begins almost immediately after detonation initiation (at $t = 0$), owing to the convergent nature of detonation propagation [19]. This is evidenced by the slope of the front tracking curve, which is slightly steeper than that of the CJ tracking during the initial period (from $t = 0$ to approximately 30).

Near the center ($r \approx 0$), significant acceleration is observed; however, the precise extent of this acceleration is difficult to discern from Fig. 4c. This observation aligns with detonation implosion experiments, where directly measuring the final velocity is challenging. In such cases, indirect methods such as measuring pressure distributions are commonly employed [20]. The velocity profiles from all three simulations exhibit similar amplitudes and trends. Notably, the radius-time plot shows that all three simulations converge at exactly the same time. In Sect. 3.1.3, the highest resolution results will be used to closely examine the flow behavior near the implosion center. For the remaining cases, a resolution of $10\,\text{pts}/\ell_{1/2}$ will be utilized to enable a parametric study without compromising the essential flow features.

3.1.3 Observations near the center

This section focuses on the final stage of the convergence process using the results from Case 3. The field of view for the zoomed soot foil in Fig. 6a is limited to a radius of 130, while Fig. 6b presents the detonation wavefront structures at several time steps leading up to the final collapse. The time interval between wavefront images, from outer to inner regions, is 0.05, and the unit length reference indicates that these fronts are extremely close to the center.

Even at the final measurable stages, with a length scale on the order of the unit length, the wavefront remains highly corrugated and does not exhibit a smooth symmetric front. This raises the question: in the inviscid limit, and without accounting for detailed thermal and physical modeling near the center, is it still reasonable to consider an ideal singularity

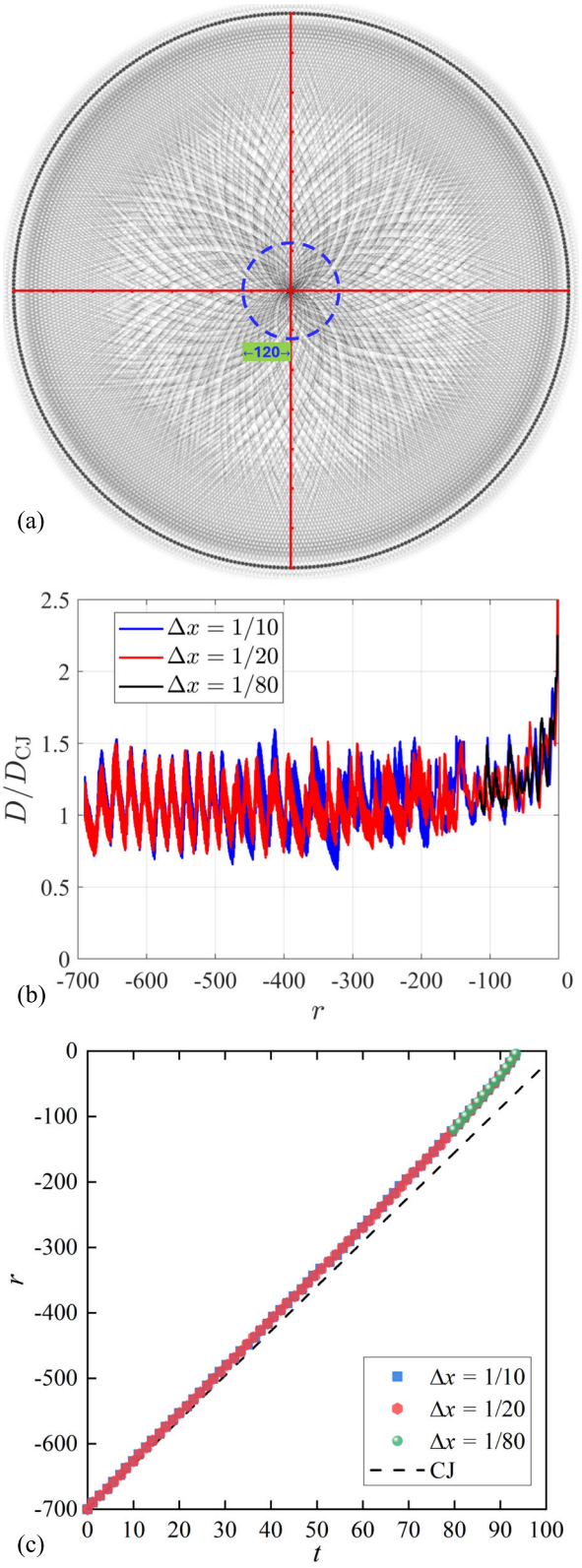

Fig. 4 Results for higher mesh resolution. **a** Soot foil for 20 pts/$\ell_{1/2}$, with the blue dashed circle indicating the refinement region for the simulation at 80 pts/$\ell_{1/2}$; **b** Instantaneous velocity along the radial direction; (**c**) Shock location versus time plot

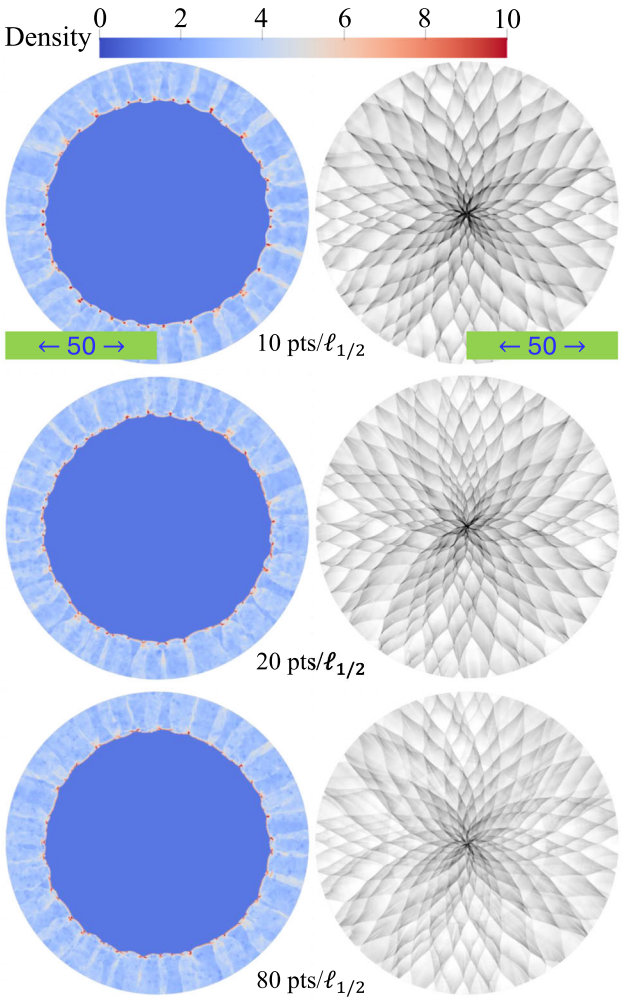

Fig. 5 Comparison of the density contours (left) at $t = 90$ and soot foil images (right) near the center, with three different mesh resolutions

for detonation implosion, or is it more accurately described as a multi-front collision phenomenon?

This idea is further supported by the soot foil in Fig. 6a, where we can trace a triple point from the outer edge to the center, as long as the mesh resolution allows. However, this conclusion is not absolute, as we cannot guarantee that similar findings would hold under all conditions. For example, for highly overdriven detonations, it is possible to encounter less unstable behaviors. Yet, it is expected that the transition from a CJ detonation to a highly overdriven detonation, where transverse instabilities settle down, requires a significant propagation distance. Previous studies [6, 7, 10, 20], as well as Fig. 4b indicate that the propagation length with significant overdrive is limited to a small portion of the domain. This suggests that an extraordinarily large domain (for simulation) or test section (for experiment) would be necessary to allow the instabilities to fully stabilize, should this phenomenon exist.

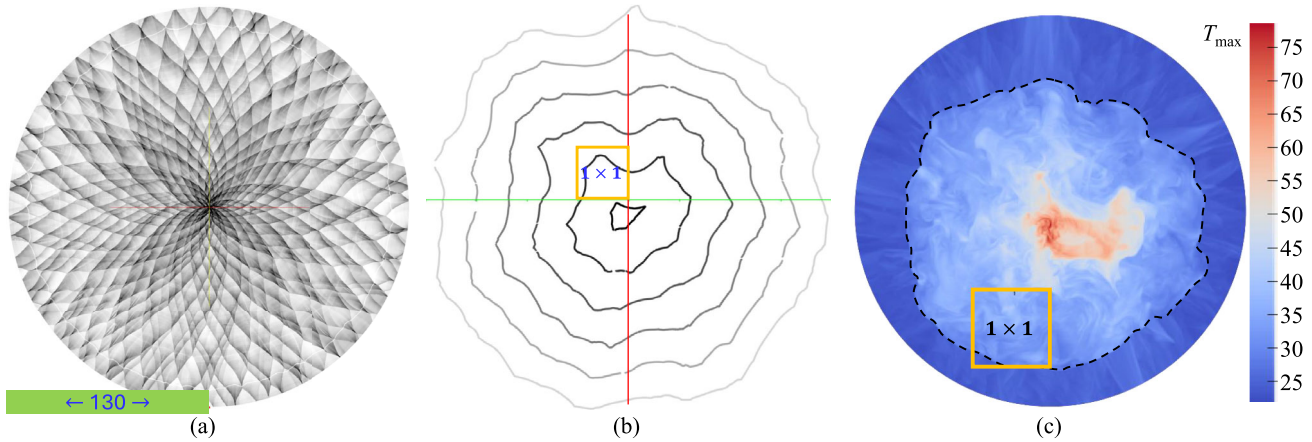

Fig. 6 Flow features very close to the center for Case 3, with the finest mesh resolution of 80 pts/$\ell_{1/2}$. The yellow boxes in **b** and **c** indicate the length reference. **a** Cellular structure near the center; **b** Wavefronts during final implosion, from outer to inner, with a time interval of 0.05 between neighboring fronts; **c** Maximum temperature recorded in each computational cell during the approach to and reflection off the center. The black dashed line represents the instantaneous wavefront of the reflected shock shortly after reflection from the center

Moreover, the thermal state can be extreme. Figure 6c presents the maximum temperature recorded in each computational cell immediately after reflection following the convergence of the detonation wave at the center. The highest value recorded for this case exceeds 78, which is higher than the value of approximately 57 recorded in Case 2 with a lower resolution. This variation in maximum temperature is expected, as the wave evolves into a randomly multi-headed structure with a high overdriven factor.

Nevertheless, the elevated temperature indicates that the assumptions of ideal gas behavior and conventional chemical equilibrium models commonly used in detonation simulations become increasingly invalid as the detonation wave approaches the global implosion center. The present study shows that the maximum temperature generally exceeds 20 (equivalent to 6000 K approximately, a typical upper limit for JANAF polynomials [21]) in a circular region with a radius of 10 length units from the center. Additionally, sporadic spots with temperatures over 20 are observed, likely due to the accelerated detonation coupled with transverse wave collisions, which occur at least 45 length units from the global implosion center.

3.2 Impact of varying ignition conditions

3.2.1 Effect of higher initiation pressure

As mentioned in Sect. 2, the parameters for the small ignition bubbles are arbitrarily chosen only to ensure that the gas can be directly detonated. Unlike wide channel detonations, where the initial ignition method plays a minor role in the final detonation characteristics, the ignition method may significantly affect the outcome in the current scenario. In cylindrical diverging detonations, varying the energy of the point ignition source can lead to direct detonation, delayed ignition, or even failure [11]. For cylindrical converging (imploding) detonations, the velocity profile over the radius has been shown to be sensitive to even small increases in initial velocity above the CJ value [7]. Therefore, it is of interest to examine the effects of modifying the initial detonation state by adjusting the parameters of the ignition bubbles.

To illustrate this concept without exhaustively covering all possibilities, a simulation with a higher initiation pressure (Case 4) is considered. The ignition bubble pressure was increased by 50%, with all other parameters remaining unchanged. The soot foil obtained is qualitatively similar to that of Case 1; therefore, the soot foil image of Case 4 is provided in Appendix 2. Figure 7 shows the velocity profiles and leading shock trajectories. As shown in Fig. 7a, due to the oscillatory nature, visually, there appears to be little difference between the velocity profiles from this initial condition and that from Case 1. However, the radius versus time plot in Fig. 7b demonstrates that the higher initiation pressure results in an earlier collapse. Aside from this, the general observations remain largely unchanged. To maintain consistency, all subsequent simulations used the same initiation pressure as in Case 1.

3.2.2 Polygonal ignition

Based on the previous findings regarding ideal cylindrical implosions, this section examines experimental setups where polygonal-like disturbances may arise. For example, in some cases, the supporting stands [9] of the test section can induce the formation of a polygonal (or near-polygonal) detonation front, or multiple ignition sources may be employed directly

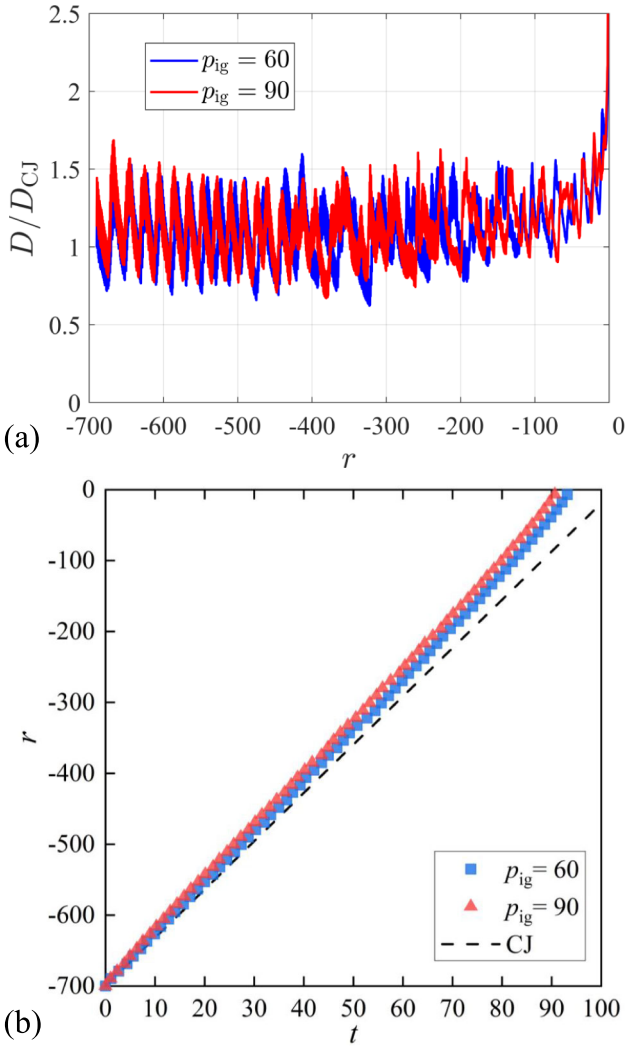

Fig. 7 Implosion with a higher ignition pressure (Case 4, 1.5 times the ignition pressure of Case 1) for the bubbles. **a** Profile of the instantaneous velocity of the wavefront; **b** Location of the wavefront as a function of time. The results of Case 1 are also shown for comparison

to generate a converging detonation [4, 22]. It is of interest to observe how these non-circular arranged sources affect the imploding process. In particular, we investigate the implosion of a polygonal detonation ignition. Simulation results for $n = 3, 6, 18$ are presented in Fig. 8, corresponding to Cases 5–7. For polygonal ignition, the shock location is measured along a line (e.g., the red dash-dot line in Fig. 8a) connecting the center of one ignition edge to the global implosion center, with the distance from any edge to the center maintained at 700 units. The wavefront structure during the implosion is shown in Appendix 1.

As background, when a shock or detonation wave interacts with a wedge, it can reflect in two ways depending on the wedge angle: regular reflection or Mach reflection (Fig. 8d). At larger wedge angles, regular reflection occurs, with the incident shock deflecting the flow and the reflected shock redirecting it so that the flow remains parallel to the wedge surface. If the wedge angle falls below a critical threshold, the reflected shock becomes too weak to restore parallel flow, leading to the formation of a third shock known as the Mach stem.

For the implosion with three ignition lines (Fig. 8a), an imaginary wedge can be defined for each ignition line, such as the top-right ignition line highlighted by the red dashed line. The corresponding schematic is shown on the left of Fig. 8d. In this case, the imaginary line perpendicular to the ignition line represents the bottom of the wedge, and the wedge's surface is formed by the symmetry of two neighboring ignition lines. The variable θ_w denotes the angle of the wedge, and the detonation propagates toward the surface of the wedge. Since this angle ($\theta_w = 60°$) exceeds the critical transition angle for detonation Mach reflection to regular reflection [23, 24], causing the detonation front to maintain a triangular shape throughout the process.

When the number of ignition lines is increased to 6 (Fig. 8b), the wedge angle is reduced to 30°, resulting in Mach reflection. The corresponding schematic is shown on the right of Fig. 8d. The Mach reflection of detonation waves has been extensively studied both experimentally by Fortin et al. [25] and numerically by Li and Lee [26, 27], including on curved surfaces [28–30]. Due to the finite characteristic length scale of the detonation, Mach reflection is a non-self-similar phenomenon. Initially, it follows a frozen limit, and at the far end, it follows an equilibrium limit. The growth rate of the Mach stem at the equilibrium limit is smaller. These observations are confirmed in the present simulation (Fig. 8b), where the trajectory of the triple point of the Mach stem is not straight, and the growth rate of the Mach stem height decreases over time. As a result, the Mach stems interact with each other during later stage. Interestingly, the detonation front remains a dodecagon for a significant amount of time (see Appendix 1 for wavefront structures during implosion).

When the number of ignition lines is increased to 18 (Fig. 8c), we observe that a cylindrical detonation front forms very early on. The soot foils for this polygonal case are quite similar to the symmetrical benchmark Case 1 when positioned away from the ignition sources. Figure 8e summarizes the radius versus time plots for various values of n, showing that the $n = 18$ case is only slightly slower than the circular case. The $n = 6$ case shows no noticeable acceleration until the final stage, while the $n = 3$ case follows the CJ detonation trajectory closely, exhibiting only regular reflections.

Figure 9 shows the Mach reflection after ignition for the $n = 18$ case discussed previously. Due to the small wedge angle ($\theta_w = 10°$), the Mach stem is less overdriven (i.e., $(V_{MS}/D_{CJ})^2 \gtrsim 1.0$, where V_{MS} is the Mach stem velocity). At $t = 30$, the triple points from neighboring Mach stems make contact. As observed in detonation Mach reflection

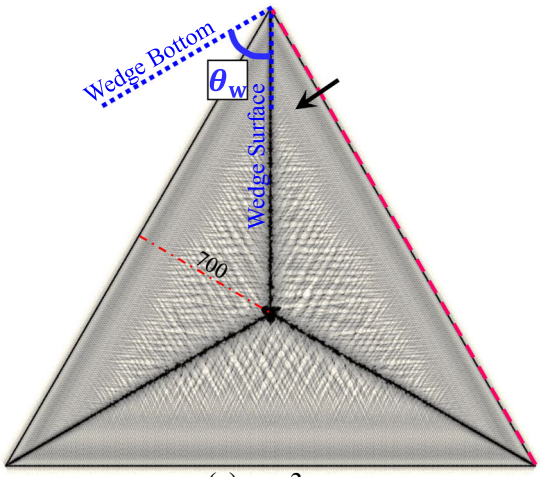

(a) $n = 3$

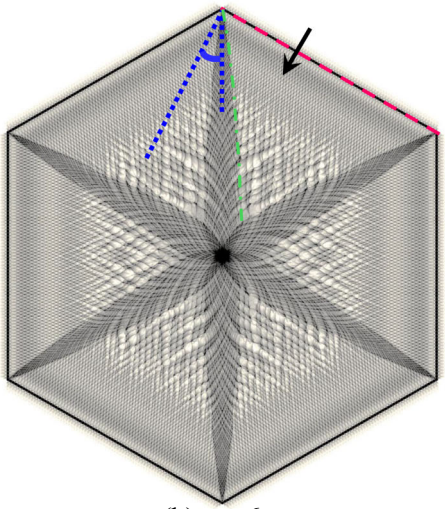

(b) $n = 6$

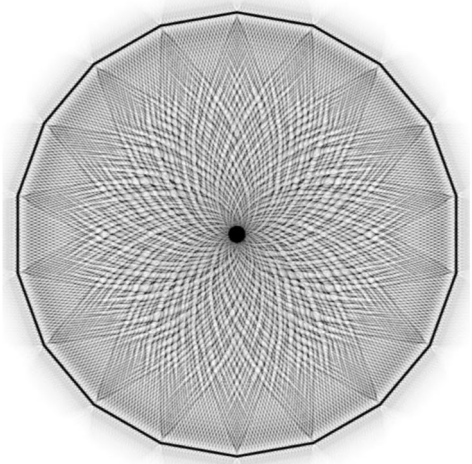

(c) $n = 18$

Fig. 8 **a**–**c** Soot foils for implosions with three different polygonal ignition sources; **d** Schematics of regular and Mach reflections with respect to **a** and **b**; **e** Detonation wavefront location as a function of time. The blue dashed lines in **a** and **b** indicate the imaginary wedge corresponding to the detonation ignited from the top-right ignition line (the red dashed line). This detonation propagates in the direction indicated by the arrow. The green dash-dot line in **b** denotes the trajectory of the triple point of the Mach stem

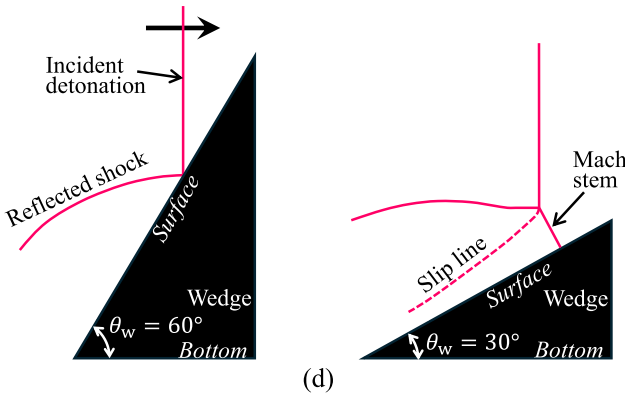

(d)

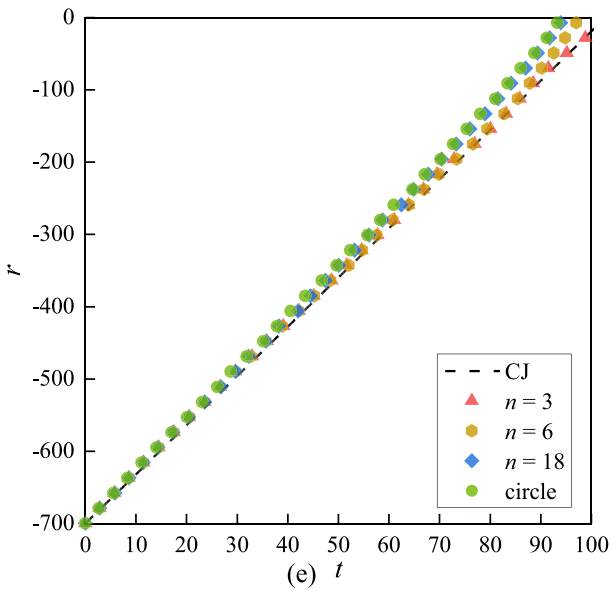

(e)

Fig. 8 continued

experiments by Fortin et al. [25], for small wedge angles, it is difficult to pinpoint the exact triple point of the Mach stem, and the front appears more curved and continuous. Our present simulation shows similar behavior: when the two triple points from neighboring Mach stems meet, the front appears continuous from an observer's perspective. This could explain why, in certain experimental setups, multiple ignition sources can still lead to a well-formed cylindrical implosion.

3.3 Implosions with obstacles or non-uniform ignition

3.3.1 General observations

Inspired by the experimental work of Knystautas and Lee [5], we artificially introduced an obstacle to disturb the wave front, as shown in Fig. 10a. A cylinder with a radius of 50 length units is placed in the path of the imploding detona-

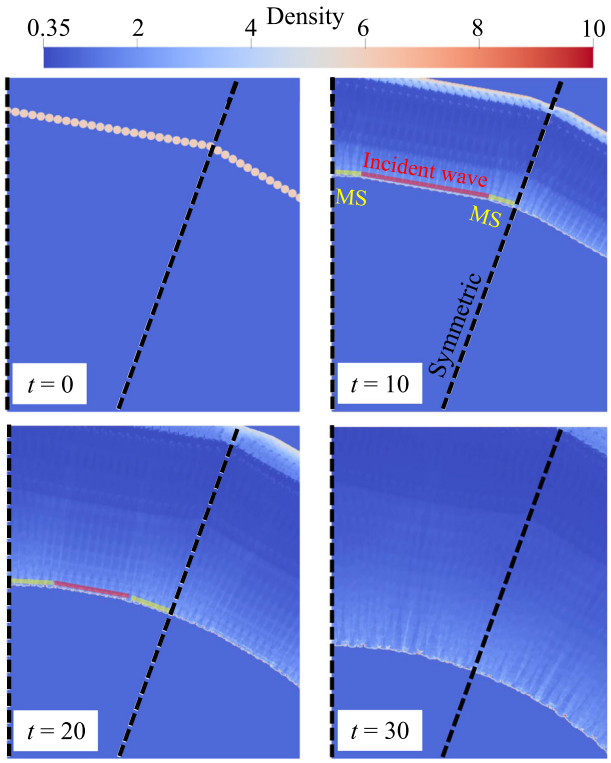

Fig. 9 Zoomed density contours showing the detonation wave structure during the initial stage of implosion ($n = 18$), including the formation and growth of the Mach stem. The black dashed lines represent the symmetry axes between two neighboring ignition lines

tion, with the center of the cylinder located 495 unit lengths away from the center (Case 9). For better visualization, the domain is rotated to examine the interaction between the cylindrical detonation wave and the obstacle in Fig. 10b. The wave reflects from the obstacle surface and, upon diffraction, the distinct cellular structures vanish in the soot foil record. We observe a higher density region where the reaction zone thickens. The wave then reflects from the line of symmetry and re-initiates the gas, coupled with a strong Mach stem that generates dense, small detonation cells. This re-acceleration causes the local wave front to catch up with the global wave front. As a result, at later stages, the wave front becomes less asymmetrical, and from the soot foil (Fig. 10a), it appears that the global implosion center remains near the center of the computational domain. It is worth noting that, similar to the experimental records by Knystautas and Lee [5], no significant shift in the global implosion center was detected when the obstacle was implemented.

3.3.2 Effects of disturbance size

This section presents results for various obstacle sizes (Cases 8–10, Fig. 11). The middle row shows a zoomed view of the soot foil near the center of the simulation, with an obstacle

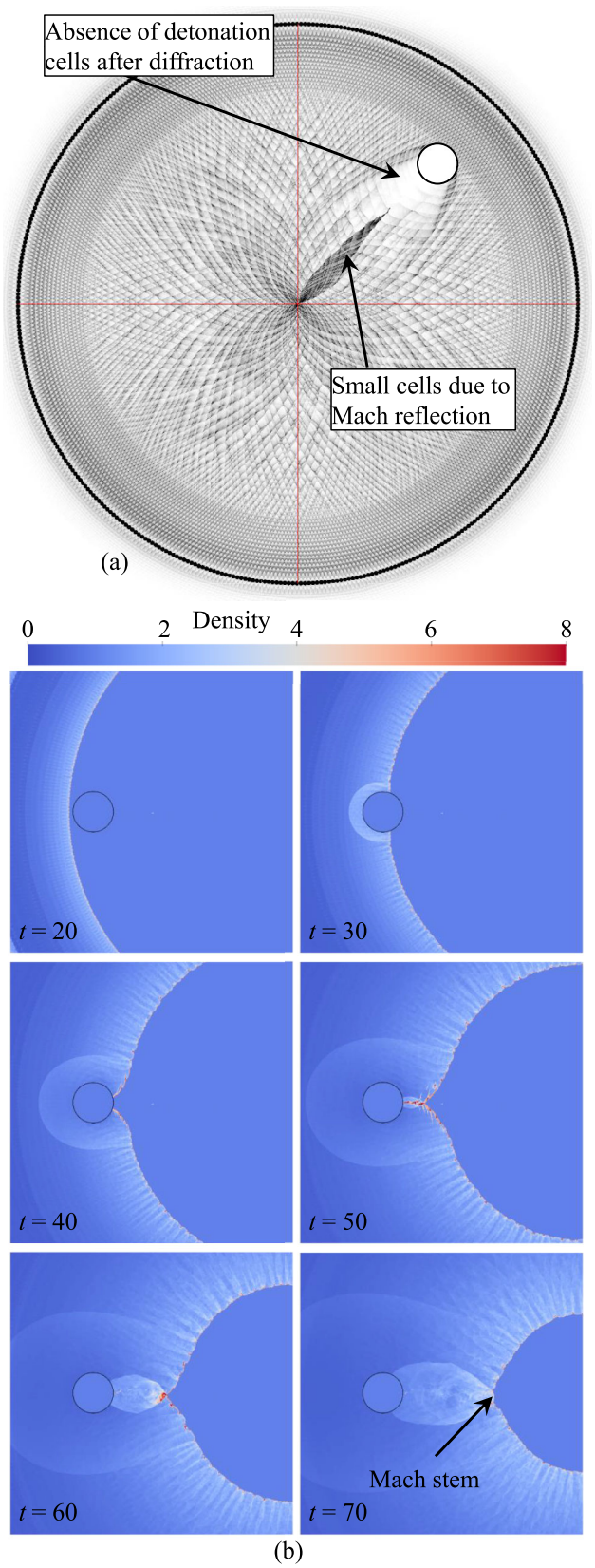

Fig. 10 Circular ignition with an obstacle of $r = 50$. **a** Soot foil; **b** Curved detonation wave front propagates over the obstacle, shown by zoomed density contours. The view is rotated for easier visualization

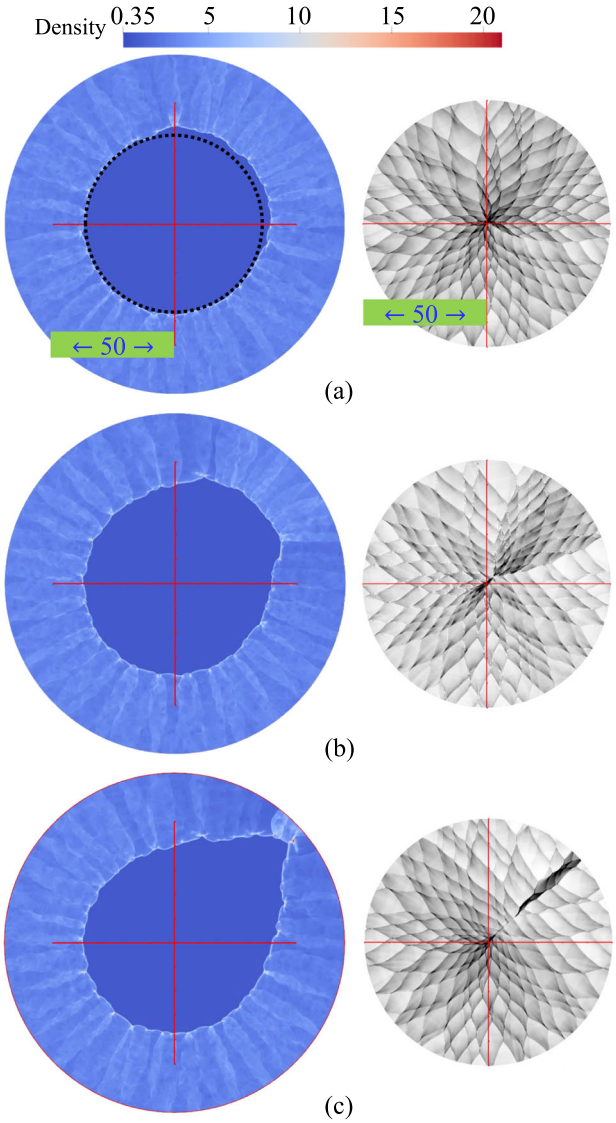

Fig. 11 Circular ignition with obstacles of varying sizes: **a** $r_{obs} = 25$; **b** $r_{obs} = 50$; **c** $r_{obs} = 100$. The left images show sample density contours before the final collision, and the right images show zoomed-in soot foils at the center. The black dot circle is used to highlight the asymmetry of the wavefront

radius of 50 units discussed in Sect. 3.3.1, as the benchmark. A slight shift in the global implosion center is visible, with the global implosion center moving toward the obstacle. The other two rows show simulations with an obstacle half the size of the radius of the benchmark case (Fig. 11a) and one that is twice the radius (Fig. 11c). For larger disturbances, the shift in the global implosion center is more pronounced, while for the smaller obstacle, the collapse still occurs near the original center.

To facilitate comparison, instantaneous wave fronts are also shown (left in Fig. 11). Even for the smallest disturbance, the distances between the wave front and the center measured along various directions, such as along the path to the

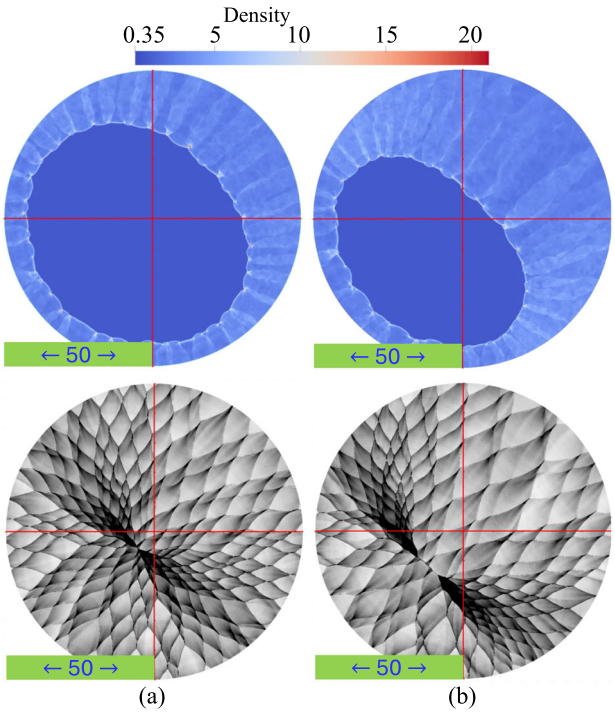

Fig. 12 Implosion with non-uniform ignition pressure. The pressure in the top-right 1/4 portion of the ignition sources is increased by **a** 50% and **b** 100% compared to the benchmark Case 1. The top shows a zoomed-in snapshot of the density contour before the final collapse, and the bottom shows a zoomed-in view of the soot foil near the center

obstacle (i.e., top-right direction) and other directions, still deviate. This suggests that the azimuthal asymmetry along the curved wave fronts persists without being fully smoothed out, rather, the apparent restoration of its former symmetry as discussed by Knystautas and Lee [5] is likely due to the limited resolution of the observation method.

Additionally, detonation implosions with polygonal ignition sources were tested with an obstacle (Cases 11 and 12). Since the observations closely align with those found for circular ignition, the results are provided in Appendix 2.

3.3.3 Effects of non-uniform ignition

In this set of cases, we increased the pressure of the ignition bubbles in the top-right portion (i.e., quadrant I). In one case, the elevated pressure is 1.5 times the original pressure (i.e., 90 unit pressure), and in the other case, it is twice the original pressure (i.e., 120 unit pressure) (Cases 13 and 14). Both simulations use polygonal ignition with $n = 18$.

The soot foil near the center and a selected snapshot of the density contour close to the center are shown in Fig. 12. Additional snapshots of wavefronts during implosion can be found in Appendix 2. Both cases show a noticeable offset in global implosion center. From the wave front at the final collapse, we observe that the second case produces a more

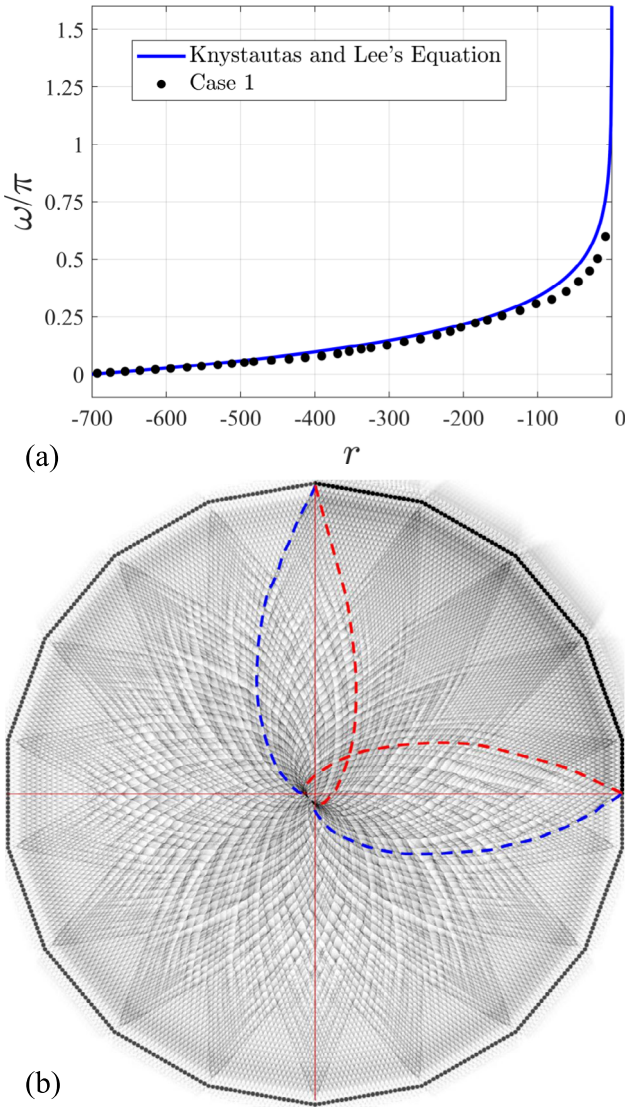

Fig. 13 **a** Angle of influence plot based on the formula by Knystautas and Lee, compared with measurements from Case 1; **b** Trajectories of triple points originating from two ignition points for the implosion with non-uniform ignition (Case 14)

elliptical wave front. In fact, the elliptical shape persists until the final collapse.

Recall from the introduction that information is believed to propagate at the speed of the transverse wave, which is close to the sound speed behind the leading shock [5]. The angle of influence relative to the center, ω, is defined as the angle formed by a point along a trajectory, the corresponding ignition point, and the center of the collapse (see Fig. 2). We plot ω as a function of the distance between the point and the center based on the derivation by Knystautas and Lee [5]:

$$\omega = \int_{R_0}^{R_s} \frac{C_1(R_s)}{D(R_s)} \frac{\mathrm{d}R_s}{R_s},$$

where $C_1(R_s)$ is the sound speed behind the shock front and $D(R_s)$ is the instantaneous detonation velocity. This formulation is based on the assumption that transverse perturbations propagate at the local sound speed. For a CJ detonation wave, the function C_1/D is constant and is given by $C_1/D = \gamma/(\gamma+1)$.

In Fig. 13a, the blue line corresponds to the approximate solution based on the CJ detonation assumption, and the actual solution, as exemplified by Case 1, closely aligns with this CJ-based solution. The result suggests that information originating from a specific point can only influence the detonation front when it is extremely close to the center. For implosions with shifts in the global implosion center, as shown in Fig. 13b, the influential zone of information carried from a point, bounded by the pair of blue and red trajectories of triple points, also remains largely constrained. Moreover, for multidimensional imploding detonations, as noted earlier, the front remains multi-headed near the center. Furthermore, tracking a transverse wave over a physically relevant length scale (i.e., one that is not microscopic such that it is significantly smaller than $\mathcal{O}(\ell_{1/2})$) indicates that a disturbance signal cannot traverse the front sufficiently to smooth out the perturbations.

It is important to emphasize that the present simulation spans a relatively large diameter in terms of the number of detonation cells, yet the detonation front near the center still exhibits strong transverse instabilities. It is well established that, in piston-supported overdriven detonations, the degree of overdrive significantly influences the propagation mode. Specifically, when the critical overdrive threshold is exceeded, the detonation transitions from an unstable to a stable propagation regime [31]; however, it might require significant distance for these instabilities to dissipate. The distance required, as well as its dependence on activation energies, remains an open question. It is hypothesized that for a sufficiently large diameter, there may be a chance for a smooth front without transverse instabilities, but this requires further investigation, as significant acceleration occurs only within a small part of the computation domain. This study provides an intuitive numerical illustration based on a mild activation energy while maintaining a reasonable computation domain size.

4 Conclusion

In this study, an imploding detonation was simulated over a sufficiently long travel distance using a classical Arrhenius reaction model with mild activation energy. For circular implosions, acceleration was observed from the onset, but significant acceleration only occurred very close to the center. When higher energy was applied to the ignition sources, the wave front reached the global implosion center earlier,

although the essential characteristics remained qualitatively unchanged.

For implosions ignited with polygonal sources, the results revealed either regular or Mach reflection of cellular detonations, depending on the number of ignition lines. In the case of regular reflection, the detonation front profiles remained consistent, and the detonation propagated close to the Chapman–Jouguet velocity without any noticeable acceleration. In contrast, the combination of Mach reflection and cellular instability facilitated a transition to a more circular shape. As the number of ignition lines increased, the wave front transitioned into a circular shape, becoming indistinguishable from that produced by circular ignition.

Simulations were carried out with a circular obstacle placed far from the center. As the obstacle size increased, the final wave front became more distorted (non-circular), and the global implosion center shifted toward the obstacle. However, this shift was minimal for smaller obstacles. A similar observation was made for implosions with non-uniform ignition pressure, where the final wave shape became elliptical. These results suggest that the smoothing effect of transverse waves alone is insufficient to eliminate disturbances. More importantly, the wave fronts remained multi-headed, even very close to the center.

However, these findings are not definitive, as accurate physical modeling of very strong imploding waves was not considered. The present results are limited to the specific parameters selected in this study, such as mild activation energy, a finite and reasonable simulation domain size, and the inviscid limit. Further research is required to better understand these phenomena.

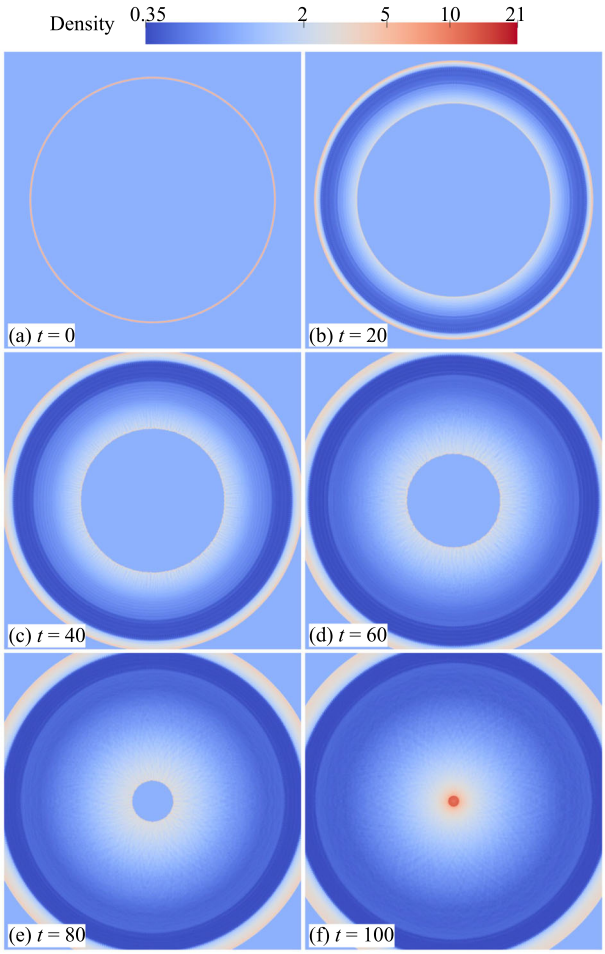

Fig. 14 Density contours illustrating the implosion process for Case 1

Appendix 1: General wave structure during circular and polygonal implosions

Figure 14 presents snapshots of density contours during the implosion process for Case 1, with a time interval of 20. The ignition hot spots form a circular pattern (Fig. 14a), triggering cellular wave fronts that implode toward the center, while relatively weak shocks propagate outward through the inert gas (Fig. 14b–e). The spacing between the transverse waves is small relative to the simulation domain, making them indistinct in the density contours, although they can be clearly observed in soot foils (Fig. 2). Finally, the waves reflect off the center in Fig. 14f.

As an alternative to the density contours for illustrating the implosion process, the entire wave front structure can be shown in a single figure for clarity and simplicity. Figure 15 displays the wave front structure during polygonal implosions.

It is noted that for $n = 6$, where Mach reflections occur but the growth rate of the Mach stem is relatively small, the wave fronts remain in a dodecagonal shape for most of the time, as seen in the colored lines highlighted in Fig. 15b at $t = 60$. In this case, the blue dashed lines represent the incident detonation waves, while the red dashed lines represent the Mach stem. Around $t = 90$, when the Mach stems interact with each other, the wave front recovers to a more hexagonal shape.

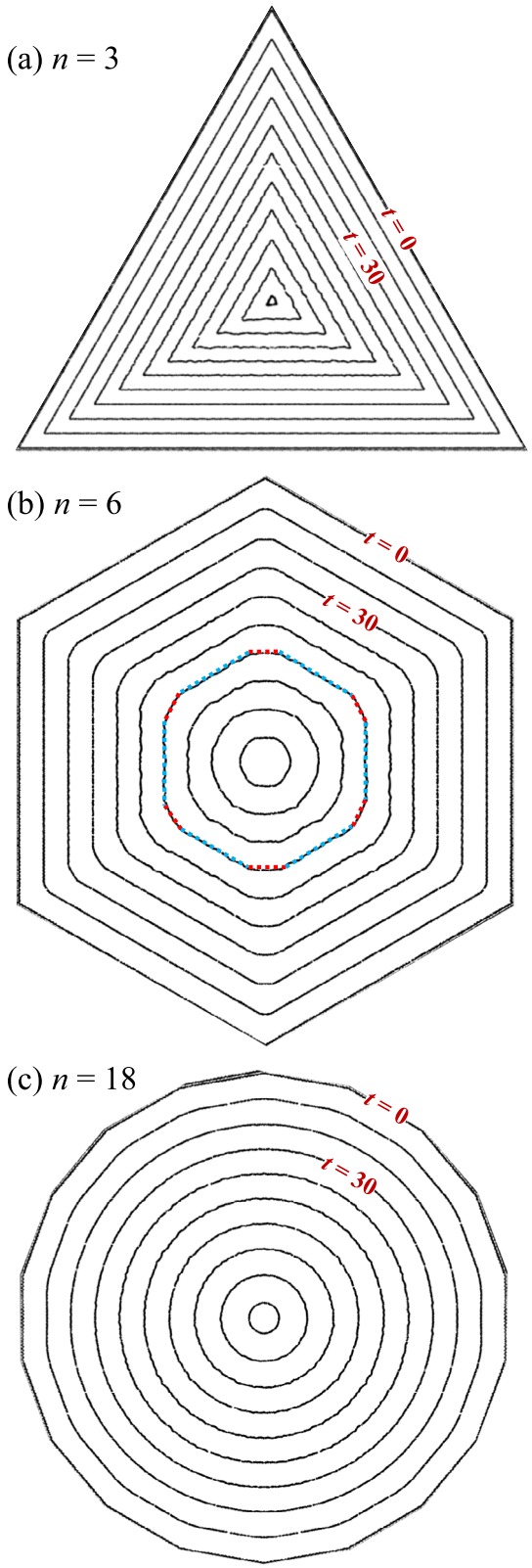

Fig. 15 Wave fronts during the implosion process for Cases 5–7, with different numbers of ignition edges: **a** n = 3; **b** n = 6; **c** n = 18. The wave fronts are shown at time intervals of 10, progressing from the outer region to the inner region. The colored dashed lines in **b** highlight the dodecagon $t = 60$

Appendix 2: Supplementary soot foils and wave structures near collapse

Figure 16 presents the numerical soot foils for cases not included in the main text.

Figure 17 illustrates the influence on polygonal implosions disturbed by an obstacle, focusing on the zoomed-in regions of Fig. 16d, e near the center. The results are qualitatively similar to those seen in circular implosions with obstacles, where the global implosion center shifts slightly toward the obstacle. Therefore, further discussion on these results is omitted in the main text.

Figure 18 shows the wave fronts near the final collapse for a polygonal implosion ($n = 18$) with non-uniform ignition pressure (Cases 13 and 14). The wave front remains cellular and does not transition to a circular shape until the collapse is complete.

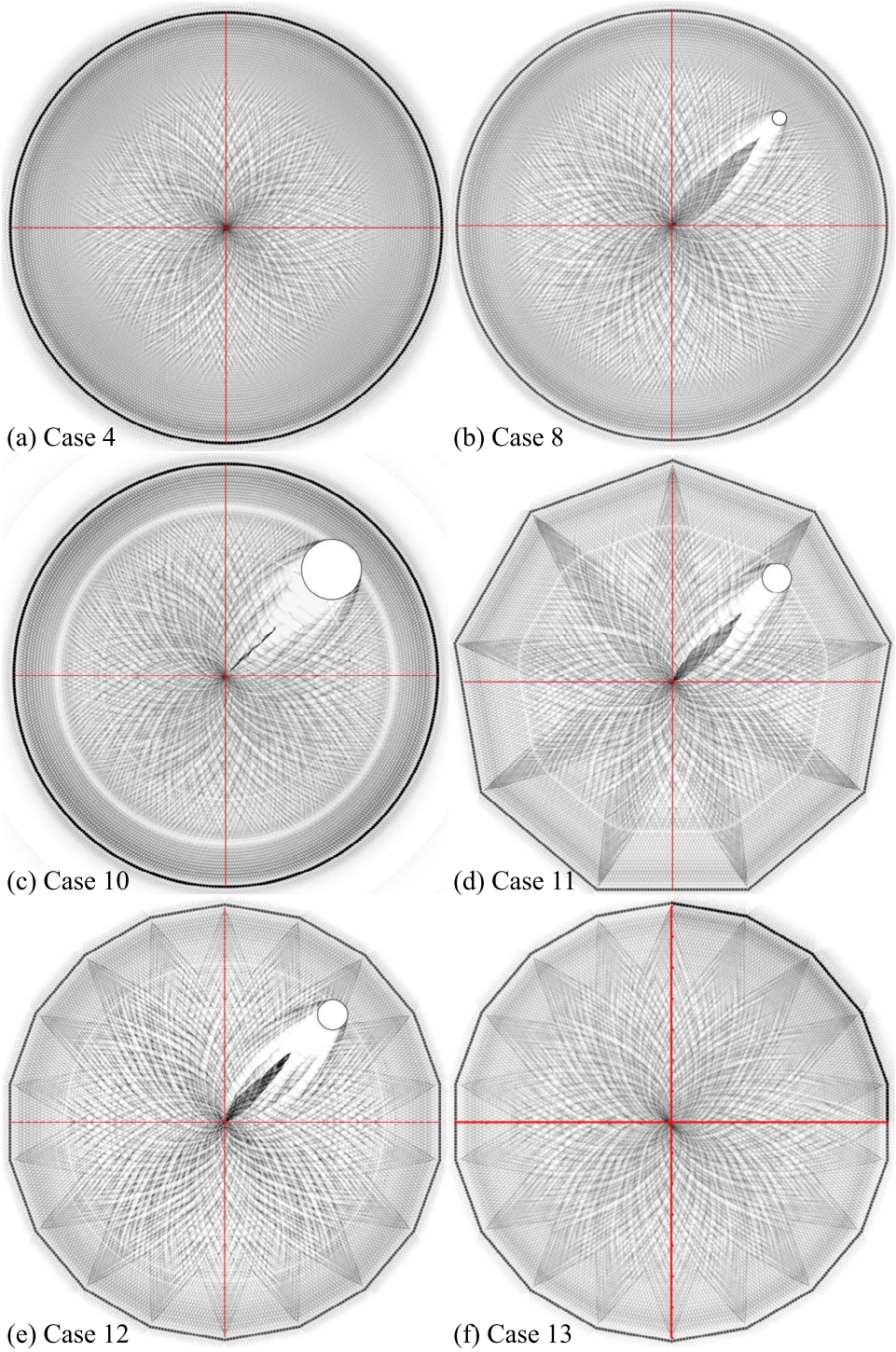

Fig. 16 Full set of numerical soot foils for cases not included in the main text

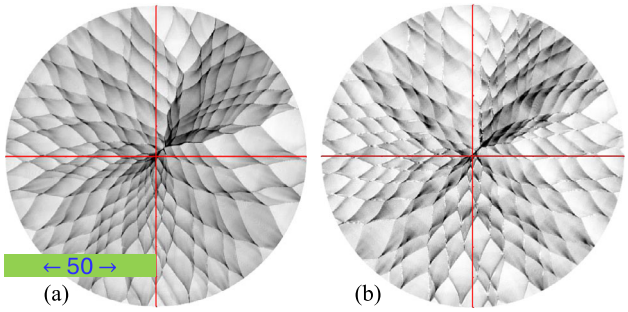

Fig. 17 Zoomed-in view of soot foils for polygonal implosions with an obstacle radius of 50: **a** $n = 9$; **b** $n = 18$

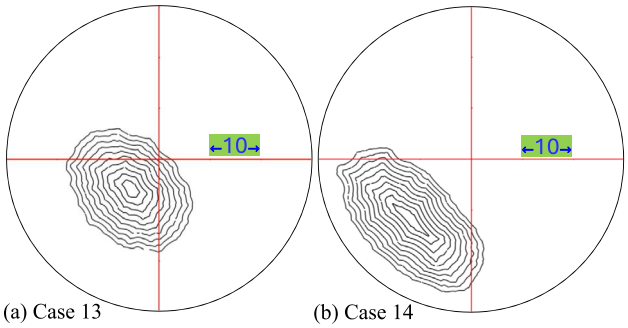

Fig. 18 Wave front structures during the final collapse for a polygonal implosion ($n = 18$) with non-uniform ignition pressure (Cases 13 and 14). From outer to inner, the time interval between neighboring fronts is 0.1

Acknowledgements L. Shi would like to thank Chaoxiong Zhang for his assistance in post-processing some of the results in this study.

Funding Open access funding provided by The Hong Kong Polytechnic University.

Data Availability Datasets generated during the current study are available from the corresponding author on reasonable request.

Declarations

Conflict of interest We have no Conflict of interest.

References

1. Kjellander, M., Tillmark, N., Apazidis, N.: Thermal radiation from a converging shock implosion. Phys. Fluids **22**(4), 046102 (2010). https://doi.org/10.1063/1.3392769
2. Apazidis, N., Kjellander, M., Tillmark, N.: High energy concentration by symmetric shock focusing. Shock Waves **23**(4), 361–368 (2013). https://doi.org/10.1007/s00193-013-0442-y
3. Lee, B.: Nonuniform propagation of imploding shocks and detonations. AIAA J. **5**(11), 1997–2003 (1967). https://doi.org/10.2514/3.4352
4. Knystautas, R., Lee, B., Lee, J.: Diagnostic experiments on converging detonations. Phys. Fluids **12**(5), 165–168 (1969). https://doi.org/10.1063/1.1692602
5. Knystautas, R., Lee, J.: Experiments on the stability of converging cylindrical detonations. Combust. Flame **16**(1), 61–73 (1971). https://doi.org/10.1016/s0010-2180(71)80012-3
6. Ahlborn, B., Huni, J.: Stability and space-time measurements of concentric detonations. AIAA J. **7**(6), 1191–1192 (1969). https://doi.org/10.2514/3.5310
7. Li, H., Ben-Dor, G.: A modified CCW theory for detonation waves. Combust. Flame **113**(1–2), 1–12 (1998). https://doi.org/10.1016/s0010-2180(97)00136-3
8. Whitham, G.: A new approach to problems of shock dynamics. Part I. Two-dimensional problems. J. Fluid Mech. **2**(2), 145–171 (1957). https://doi.org/10.1017/s002211205700004x
9. Rodriguez Rosero, S., Loiseau, J., Higgins, A.J.: Asymmetry of imploding detonations in thin channels. Shock Waves **34**(5), 413–427 (2024). https://doi.org/10.1007/s00193-024-01196-z
10. Oran, E.S., DeVore, C.R.: The stability of imploding detonations: results of numerical simulations. Phys. Fluids **6**(1), 369–380 (1994). https://doi.org/10.1063/1.868092
11. Shen, H., Parsani, M.: The role of multidimensional instabilities in direct initiation of gaseous detonations in free space. J. Fluid Mech. **813**, R4 (2017). https://doi.org/10.1017/jfm.2017.5
12. Han, W., Kong, W., Law, C.K.: Propagation and failure mechanism of cylindrical detonation in free space. Combust. Flame **192**, 295–313 (2018). https://doi.org/10.1016/j.combustflame.2018.01.049
13. Mi, X., Higgins, A.J., Kiyanda, C.B., Ng, H.D., Nikiforakis, N.: Effect of spatial inhomogeneities on detonation propagation with yielding confinement. Shock Waves **28**(5), 993–1009 (2018). https://doi.org/10.1007/s00193-018-0847-8
14. Shi, L., Wen, C.-Y., Sun, X., Fan, E.: Detonation propagation in continuously curved three-dimensional ducts. Combust. Flame **280**, 114363 (2025). https://doi.org/10.1016/j.combustflame.2025.114363
15. Frahan, M.T., Rood, J.S., Day, M.S., Sitaraman, H., Yellapantula, S., Perry, B.A., Grout, R.W., Almgren, A., Zhang, W., Bell, J.B., Chen, J.H.: PeleC: An adaptive mesh refinement solver for compressible reacting flows. Int. J. High Perform. Comput. Appl. **37**(2), 115–131 (2023). https://doi.org/10.1177/10943420221121151
16. Colella, P., Woodward, P.R.: The piecewise parabolic method (PPM) for gas-dynamical simulations. J. Comput. Phys. **54**(1), 174–201 (1984). https://doi.org/10.1016/0021-9991(84)90143-8
17. Nonaka, A., Day, M.S., Bell, J.B.: A conservative, thermodynamically consistent numerical approach for low Mach number combustion. Part I: single-level integration. Combust. Theor. Model. **22**(1), 156–184 (2018). https://doi.org/10.1080/13647830.2017.1390610
18. Sharpe, G., Radulescu, M.: Statistical analysis of cellular detonation dynamics from numerical simulations: one-step chemistry. Combust. Theor. Model. **15**(5), 691–723 (2011). https://doi.org/10.1080/13647830.2011.558594
19. Akbar, R., Schwendeman, D., Shepherd, J., Williams, R., Thomas, G.: Wave shaping channels for gaseous detonations. In: Shock Waves@ Marseille IV: Shock Structure and Kinematics, Blast

Waves and Detonations, pp. 465–470. Springer, Berlin (1995). https://doi.org/10.1007/978-3-642-79532-9_77
20. Lee, J.H., Lee, B.H.: Cylindrical imploding shock waves. Phys. Fluids **8**(12), 2148–2152 (1965). https://doi.org/10.1063/1.1761173
21. Chase, M.W.: NIST-JANAF Thermochemical Tables, 4th edn. American Institute of Physics, Providence (1998)
22. Ishii, K., Ueo, H.: Behavior of imploding detonation waves in a cylindrical chamber. 30th International Colloquium on the Dynamics of Explosions and Reactive Systems, Ottawa, Canada (2025). https://icders.com/res/ICDERS2025-162.pdf
23. Meltzer, J., Shepherd, J.E., Akbar, R., Sabet, A.: Mach reflection of detonation waves. In: Kuhl A.L., Leyer J.C., Borisov A.A., Sirignano W.A. (eds.) Progress in Astronautics and Aeronautics, vol. 153, pp. 78–94. AIAA, New York (1993). https://doi.org/10.2514/5.9781600866265.0078.0094
24. Li, J., Ren, H., Wang, X., Ning, J.: Length scale effect on Mach reflection of cellular detonations. Combust. Flame **189**, 378–392 (2018). https://doi.org/10.1016/j.combustflame.2017.11.002
25. Fortin, Y., Liu, J., Lee, J.H.: Mach reflection of cellular detonations. Combust. Flame **162**(3), 819–824 (2015). https://doi.org/10.1016/j.combustflame.2014.09.003
26. Li, J., Ning, J., Lee, J.: Mach reflection of a ZND detonation wave. Shock Waves **25**(3), 293–304 (2015). https://doi.org/10.1007/s00193-015-0562-7
27. Li, J., Lee, J.: Numerical simulation of Mach reflection of cellular detonations. Shock Waves **26**(5), 673–682 (2016). https://doi.org/10.1007/s00193-016-0668-6
28. Li, J., Ning, J.: Experimental and numerical studies on detonation reflections over cylindrical convex surfaces. Combust. Flame **198**, 130–145 (2018). https://doi.org/10.1016/j.combustflame.2018.07.017
29. Wang, L., Ma, H.: Detonation wave reflection over a concave-convex cylindrical wedge. Shock Waves **34**(3), 285–289 (2024). https://doi.org/10.1007/s00193-024-01176-3
30. Shi, L., Zhang, Z., Fan, E., Wen, C.-Y.: Simulations of detonation wave reflection over cylindrical convex surfaces with a detailed reaction model. Phys. Fluids **37**(8), 081705 (2025). https://doi.org/10.1063/5.0285327
31. He, L., Lee, J.H.: The dynamical limit of one-dimensional detonations. Phys. Fluids **7**(5), 1151–1158 (1995). https://doi.org/10.1063/1.868556